

# Non-collinear magnetic structures in the magnetoelectric Swedenborgite $\text{CaBaFe}_4\text{O}_7$ derived by powder and single-crystal neutron diffraction

N. Qureshi<sup>1,2\*</sup>, B. Ouladdiaf<sup>1</sup>, A. Senyshyn<sup>3</sup>, V. Caignaert<sup>4</sup>, M. Valldor<sup>5,2</sup>

**1** Institut Laue-Langevin, Grenoble, France

**2** II. Physikalisches Institut, Universität zu Köln, Germany

**3** Forschungs-Neutronenquelle Heinz Maier-Leibnitz (FRM-II), Technische Universität München, Garching, Germany

**4** CRISMAT, UMR 6508, CNRS-ENSICAEN, Caen, France

**5** Centre for Materials Science and Nanotechnology (SMN), Department of Chemistry, University of Oslo, Norway

\* qureshi@ill.fr

December 16, 2021

## Abstract

We have investigated the magnetic structures of the Swedenborgite compound  $\text{CaBaFe}_4\text{O}_7$  using magnetic susceptibility and neutron diffraction experiments on powder and single-crystal samples. Below  $T_{N1} = 274$  K the system orders in a ferrimagnetic structure with spins along the  $c$  axis and an additional antiferromagnetic component within the kagome plane which obviously cannot satisfy all exchange interactions. Competing single-ion anisotropy and exchange interactions lead to a transition into a multi-q conical structure at  $T_{N2} = 202$  K. The derivation of the complex ordering scheme below  $T_{N2}$  is an important step towards the understanding of the magnetoelectric effect under magnetic fields in this polar ferrimagnet.

---

## Contents

<b>1</b>	<b>Introduction</b>	<b>2</b>
<b>2</b>	<b>Experimental</b>	<b>4</b>
<b>3</b>	<b>Results</b>	<b>4</b>
3.1	Single-crystal measurements	4
3.1.1	Nuclear structure	4
3.1.2	Magnetic phase transitions	5
3.1.3	Magnetic structures	7
3.2	Powder neutron diffraction	11
<b>4</b>	<b>Conclusion</b>	<b>16</b>
	<b>References</b>	<b>17</b>

---

## 39 1 Introduction

40 Geometrical frustration [1, 2] occurs in lattices of vertex-sharing triangles, e.g. kagome  
 41 layers [3, 4] or pyrochlore nets [5, 6], in which the antiferromagnetic exchange interactions  
 42 of nearest neighbours cannot be satisfied. Crystal structures with a high degree of frustra-  
 43 tion, e.g. a network of equilateral triangles, may not reveal a long-range ordered magnetic  
 44 ground state even down to very low temperatures. However, small distortions from the  
 45 high-symmetry crystal structures allow the spin system to order in interesting and exotic  
 46 ways.

47 The magnetic Swedenborgites, with its first member reported as  $\text{YBaCo}_4\text{O}_7$  in 2002 [7],  
 48 are structural homologues to the hexagonal mineral  $\text{SbNaBe}_4\text{O}_7$  [8, 9], and are extensively  
 49 studied due to their interesting crystal structures and diverse magnetic properties. The  
 50 first observations from the magnetic lattice of hexagonal  $\text{YBaCo}_4\text{O}_7$ , i.e. diffuse neutron  
 51 scattering on powder, suggested only short range spin order [7]. By diluting its magnetic  
 52 lattice with a non-magnetic ion in  $\text{YBa}(\text{Co}_{4-x}\text{Zn}_x)\text{O}_7$  ( $x = 0-3$ ) the properties gradu-  
 53 ally change into a spin-glass [7, 10]. In the orthorhombically distorted Swedenborgite  
 54  $\text{YbBaCo}_4\text{O}_7$ , a long-range order was indicated with sharp Bragg reflections in neutron  
 55 diffraction experiments, however, only the propagation vectors could be identified and not  
 56 the full spin structure [11]. Simultaneously, it became obvious that the oxygen stoichiom-  
 57 etry was important for the resulting symmetry of the atomic lattice in the Swedenbor-  
 58 gites [12]. Additionally, the single-ion anisotropy (magnetocrystalline) effects apparently  
 59 affect the symmetry and magnetism. In  $\text{CaBaCo}_4\text{O}_7$ , having a  $\text{Co}^{2+}/\text{Co}^{3+}$  ratio of 1, the  
 60 atomic lattice is orthorhombic and a ferrimagnetic-like ground state was reported [13, 14].  
 61 In the subject of this study -  $\text{CaBaFe}_4\text{O}_7$ , with a similar charge composition - the Swe-  
 62 denborgite lattice is also orthorhombically distorted and a long-range spin order appears  
 63 already close to room temperature [15, 16]. Magnetocurrent measurements revealed the  
 64 magnetoelectric effect under the application of an external magnetic field for which a non-  
 65 collinear and non-coplanar spin order was claimed to be responsible [17], therefore making  
 66 the link to the highly interesting material class of multiferroics [18, 19]. However, no neu-  
 67 tron diffraction study devoted to the details of the involved magnetic structure exists in  
 68 the literature, which is the main motivation for the investigation presented below.

69 The actual, magnetic ground states in the Swedenborgite systems strongly depend on the  
 70 type of structural distortion away from the hexagonal symmetry, which releases the geo-  
 71 metric frustration to some degree and allows for a magnetic state with several, similarly  
 72 strong, but competing spin interactions. Also, with the uneven distribution of electrons  
 73 among the  $d$  orbitals in tetrahedral crystal fields in the Swedenborgite structure, contri-  
 74 butions from Jahn-Teller-like single-ion anisotropy would be valid for  $d^6$  ions like  $\text{Fe}^{2+}$   
 75 and  $\text{Co}^{3+}$ , of which the former is present here. However, with the present data it will  
 76 not be possible to exclusively relate the magnetic properties with the local electric phe-  
 77 nomena, but those investigations could be very important for the future understanding of  
 78 spin-ordering phenomena in Swedenborgites.

79 According to the Mermin-Wagner [20] theorem, a 1D or 2D isotropic spin-S Heisenberg  
 80 model cannot reveal long-range order. Although magnetocrystalline anisotropy is expected  
 81 for the  $\text{Fe}^{2+}$  ( $d^6$ ) ion [the  $\text{Fe}^{3+}$  ( $d^5$ ) spin is symmetrical in tetrahedral crystal fields], a  
 82 significant magnetic coupling between the kagome layers is probably an important factor  
 83 for the magnetic properties in Swedenborgites. Therefore, the triangular layer of magnetic  
 84 ions between the kagome layers, see Figure 1(a) for the case of  $\text{CaBaFe}_4\text{O}_7$ , plays a de-  
 85 cisive role for the appearance of long-range order in these systems as it can mediate the  
 86 spin-spin interaction leading to a 3D spin system.

87 By viewing the crystal structure along the  $c$  axis [Figure 1(b)] it can be seen that

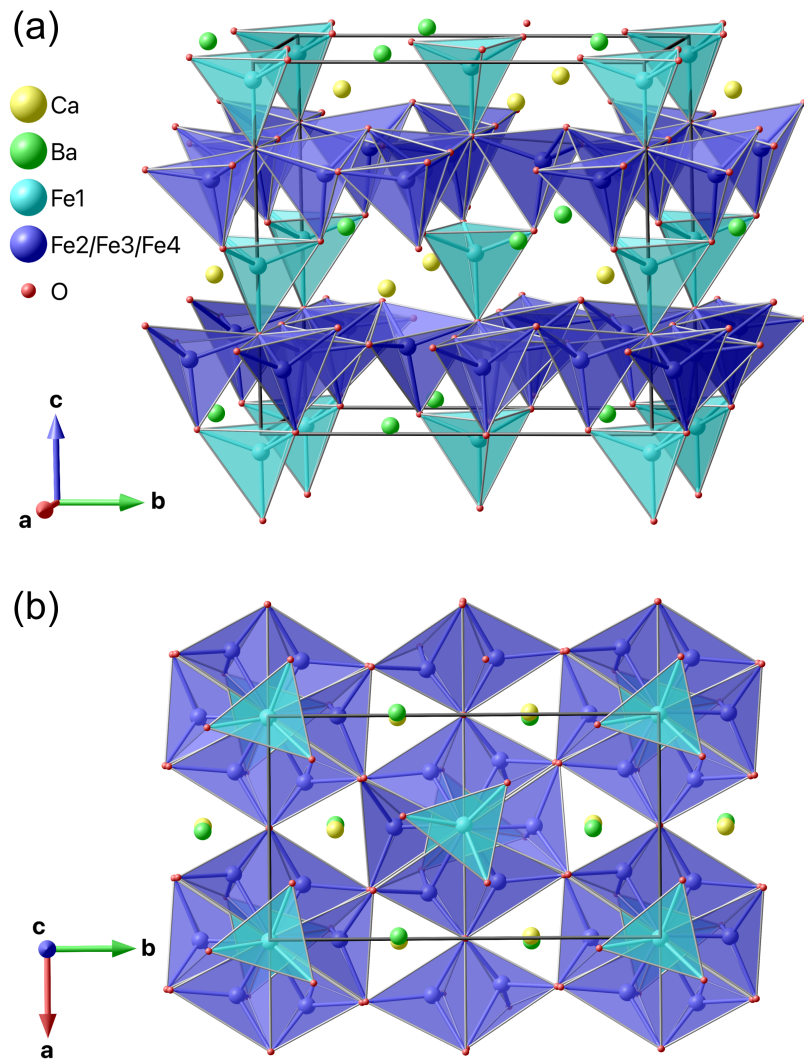


Figure 1: (a) Visualization of the crystal structure of  $\text{CaBaFe}_4\text{O}_7$  consisting of triangular Fe sites (light blue) and hexagonal Fe sites (dark blue), where the latter form the kagome planes within the  $a$ - $b$  plane. (b) View along the  $c$  axis emphasizing the close-to hexagonal symmetry and the two different types of triangles within the kagome planes as described in the text.

each kagome layer reveals two different types of triangles: the first type of triangle ( $T_1$ ) is situated around the vertical connection between two Fe spins of the triangular plane, while the second type of triangles ( $T_2$ ) surrounds either a Ca or Ba cation. In the present study, neutron diffraction experiments on powder and single-crystal samples reveal the magnetic structures of the  $\text{CaBaFe}_4\text{O}_7$  compound which offer an interesting insight into the exchange couplings between the planes and especially within the two different types of triangles of the kagome planes.

## 2 Experimental

The synthesis of powders and growth of single crystalline  $\text{CaBaFe}_4\text{O}_7$  is described in detail elsewhere [16]. In short, single crystals ( $> 1$  cm) were grown in an optical floating-zone furnace. Pieces of the single crystal were ground into powder to assure that all data, presented here, correspond to the same sample.

The magnetic susceptibility measurements were done with a vibrating sample magnetometer (VSM, 40 Hz, 2mm) in a physical property measurement system (PPMS, Quantum Design) by cooling under an applied magnetic field of  $\mu_0 H = 1$  T. All susceptibility data shown here were taken from [16]. Powder neutron diffraction data [21] was obtained at SPODI (FRM II, Munich, Germany) [22], using a constant wavelength of 2.537 Å. About 20 grams of sample powder was placed in a sample holder of vanadium and the cryostat walls were all of aluminum. Helium was used as cooling agent in a top-loading closed-cycle refrigerator from Vericold. Diffraction patterns were recorded at 15 K and 300 K as well as in 15 K steps between 105 K and 270 K. The neutron single-crystal diffraction experiment [21] was carried out at the D10 diffractometer (ILL, Grenoble) in the four-circle geometry. A single-crystal specimen of  $3 \times 3.5 \times 4$  mm<sup>3</sup> (along the  $a$ ,  $b$  and  $c$  axes) was used. The nuclear structure was investigated using two different wavelengths, one being  $\lambda_1 = 2.36$  Å employed from the (002) reflection of a HOPG monochromator and the other  $\lambda_2 = 1.26$  Å from the (200) reflection of a Cu monochromator. All integrated intensities were corrected for absorption applying the transmission factor integral  $\exp[-\mu(\tau_{in} + \tau_{out})]$  by using MAG2POL [23] ( $\tau_{in}$  and  $\tau_{out}$  represent the path lengths of the beam inside the crystal before and after the diffraction process,  $\mu$  is the linear absorption coefficient, which is  $0.0056$  mm<sup>-1</sup> for  $\text{CaBaFe}_4\text{O}_7$  at  $\lambda_1$  and  $0.0096$  mm<sup>-1</sup> at  $\lambda_2$ , respectively).

The powder diffraction data were analyzed using the FULLPROF [24] package, while all single-crystal diffraction data were treated with MAG2POL [23].

## 3 Results

### 3.1 Single-crystal measurements

#### 3.1.1 Nuclear structure

We have investigated the nuclear structure at RT by collecting 722 and 119 symmetry-inequivalent reflections (1541 and 996 unique reflections) at  $\lambda_1$  and  $\lambda_2$ , respectively. Apart from two scale factors, one for each data set, the refined parameters were the atomic positions, the isotropic temperature factors (constrained to be equal for same elements on different sites) and the diagonal elements of the extinction correction tensor within an empirical SHELX-like model [25]. The refinement returned acceptable agreement factors of  $R_{F,1} = 10.9$  and  $R_{F,2} = 5.9$  for the two data sets with  $\lambda_1$  and  $\lambda_2$ , respectively.

Since the orthorhombic Swedenborgite crystal structure is very closely related to the undis-



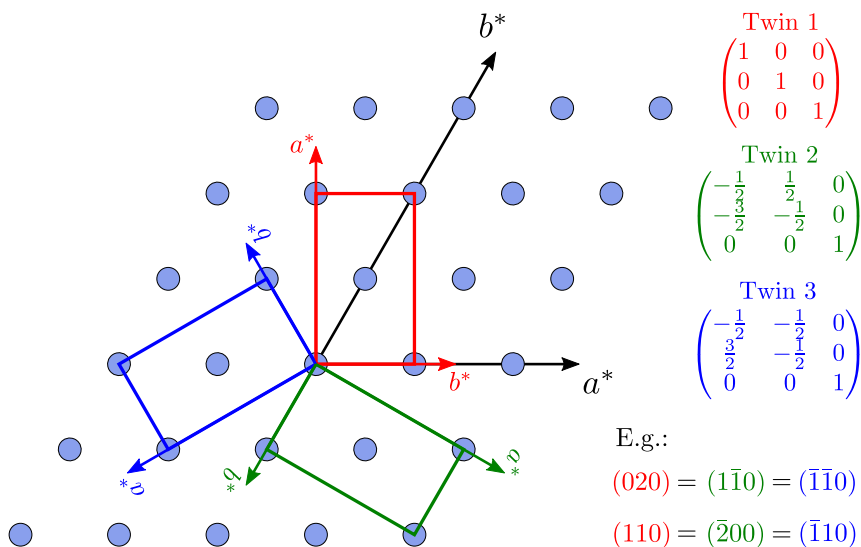


Figure 2: Sketch of the reciprocal space showing 3 twins rotated by  $120^\circ$  as a consequence from a high-temperature structural transition from a hexagonal to an orthorhombic structure. The actually observed scattering vectors  $\mathbf{Q}$  are obtained by multiplying the twin matrices by the nominal  $\mathbf{Q}$  vector of twin 1.

131 torted hexagonal structure of  $\text{SbNaBe}_4\text{O}_7$  and the  $\text{CaBaFe}_4\text{O}_7$  compound reveals a trigonal  
 132 symmetry at higher temperatures [26], we have repeated the structural analysis by includ-  
 133 ing 3 orthorhombic twins being rotated by  $120^\circ$  degrees as shown in Figure 2 and by  
 134 refining their populations. The inclusion of twins reveals a significant improvement of the  
 135 refinement quality, which is expressed by  $R_{F,1} = 4.7$  and  $R_{F,2} = 2.9$ , and the presence of a  
 136 perfectly twinned sample with homogeneously distributed twins. The refined parameters  
 137 are shown in Table 1.

### 138 3.1.2 Magnetic phase transitions

139 Figure 3(a) shows the susceptibility curves as a function of temperature for an applied  
 140 field of  $H = 1$  T applied either parallel or perpendicular to the  $c$  axis of the Swedenborgite  
 141 structure. As this strong magnetic anisotropy already appears far above the first magnetic  
 142 ordering temperature, i.e. in the paramagnetic range, it might be argued that single-ion  
 143 anisotropy is present in the system.  $\text{Fe}^{2+}$  ( $d^6$  ion) in a tetrahedral crystal field obviously  
 144 allows for a local preferred orientation of its magnetic spin. However, without further data,  
 145 it is only possible to speculate on how significant this contribution is to the spin ordering  
 146 phenomenon. At  $T_{N1} = 274$  K a local maximum is visible in the  $H \perp c$  curve, while the  
 147  $H \parallel c$  curve reveals a large increase of  $\chi$  upon cooling indicative of a ferro- or ferrimagnetic  
 148 structure with magnetic moments along the  $c$  axis with an additional antiferromagnetic  
 149 component perpendicular to  $c$ . The anomaly at  $T_{N2} = 202$  K visible only in the  $H \parallel c$   
 150 curve suggests a spin reorientation of the in-plane component.

151 The integrated intensities of selected Bragg reflections from the single-crystal neutron  
 152 diffraction experiment are depicted in Figure 3(b) on the same temperature scale. Clear  
 153 anomalies coincide with the transition temperatures observed in the magnetic susceptibil-  
 154 ity. On cooling through  $T_{N1}$  a strong increase of intensity is seen in the (020) and (110)  
 155 reflections, while only a moderate increase is present in the (002) reflection. Since only the  
 156 perpendicular component of the ordered magnetic moment with respect to the scattering  
 157 vector  $\mathbf{Q}$  contributes to magnetic scattering the intensity evolution suggests a predominant  
 158 alignment of the spins parallel to the  $c$  axis with a smaller in-plane component, in perfect

Table 1: Refined nuclear structure parameters within the  $Pbn2_1$  space group at RT ( $R_{F,1} = 4.7$ ,  $R_{F,2} = 2.9$ ,  $\chi^2 = 4.3$ ). The only Wyckoff site in this space group is the general  $4a$  site. Note that not all atomic positions can be refined at the same time due to the absence of a special position, i.e. the origin needs to be fixed. The extinction parameters  $x_{ii}$  are the diagonal entries of a tensor used to calculate the extinction factor. Note that the isotropic temperature factor  $B$  has been constrained to be the same for elements on different sites.

Atoms	$x$	$y$	$z$	$B$ ( $\text{\AA}^2$ )
Ca	0.011(3)	0.6686(6)	0.8915(8)	0.69(8)
Ba	0.001(2)	0.6696(5)	0.5203(9)	1.39(5)
Fe1	0.001(2)	0.000(2)	0.9516(8)	0.82(1)
Fe2	0.003(2)	0.1782(2)	0.6997(8)	0.82
Fe3	0.2935(5)	0.0934(3)	0.1941(9)	0.82
Fe4	0.2471(5)	0.9139(4)	0.7007(8)	0.82
O1	0.001(2)	0.003(2)	0.2665(8)	1.05(2)
O2	0.004(2)	0.5007(3)	0.2562(9)	1.05
O3	0.7835(8)	0.2633(5)	0.8053(9)	1.05
O4	0.7180(7)	0.7531(6)	0.2244(9)	1.05
O5	0.054(1)	0.1565(4)	0.514(1)	1.05
O6	0.1958(9)	0.1102(5)	0.019(1)	1.05
O7	0.2508(9)	0.9402(4)	0.516(1)	1.05

Lattice parameters  
 $a = 6.3135 \text{ \AA}$     $b = 11.0173 \text{ \AA}$     $c = 10.3497 \text{ \AA}$

Extinction parameters  
 $x_{11} = 0.005(2)$     $x_{22} = -0.0005(3)$     $x_{33} = 0.0013(1)$

Twin populations  
twin 1: 0.337   twin 2: 0.328(7)   twin 3: 0.335(8)

Table 2: Basis vectors  $\psi_n$  of the irreducible representation  $\Gamma_n$  for each of the Fe sites of  $\text{CaBaFe}_4\text{O}_7$  for space group  $Pbn2_1$  and propagation vector  $\mathbf{q} = (0\ 0\ 0)$ .

Atom	Position	$\psi_1$	$\psi_2$	$\psi_3$	$\psi_4$
1	$\begin{pmatrix} x \\ y \\ z \end{pmatrix}$	$\begin{pmatrix} u \\ v \\ w \end{pmatrix}$	$\begin{pmatrix} u \\ v \\ w \end{pmatrix}$	$\begin{pmatrix} u \\ v \\ w \end{pmatrix}$	$\begin{pmatrix} u \\ v \\ w \end{pmatrix}$
2	$\begin{pmatrix} \bar{x} \\ \bar{y} \\ z + 1/2 \end{pmatrix}$	$\begin{pmatrix} \bar{u} \\ \bar{v} \\ w \end{pmatrix}$	$\begin{pmatrix} \bar{u} \\ \bar{v} \\ w \end{pmatrix}$	$\begin{pmatrix} u \\ v \\ \bar{w} \end{pmatrix}$	$\begin{pmatrix} u \\ v \\ \bar{w} \end{pmatrix}$
3	$\begin{pmatrix} \bar{x} + 1/2 \\ \bar{y} + 1/2 \\ z \end{pmatrix}$	$\begin{pmatrix} u \\ \bar{v} \\ \bar{w} \end{pmatrix}$	$\begin{pmatrix} \bar{u} \\ v \\ w \end{pmatrix}$	$\begin{pmatrix} u \\ \bar{v} \\ \bar{w} \end{pmatrix}$	$\begin{pmatrix} \bar{u} \\ v \\ w \end{pmatrix}$
4	$\begin{pmatrix} x + 1/2 \\ \bar{y} + 1/2 \\ z + 1/2 \end{pmatrix}$	$\begin{pmatrix} \bar{u} \\ v \\ \bar{w} \end{pmatrix}$	$\begin{pmatrix} u \\ \bar{v} \\ w \end{pmatrix}$	$\begin{pmatrix} u \\ \bar{v} \\ w \end{pmatrix}$	$\begin{pmatrix} \bar{u} \\ v \\ \bar{w} \end{pmatrix}$

159 agreement with the interpretation of the susceptibility curves. At  $T_{N2} = 204$  K the (002)  
 160 reflection - being sensitive only to the in-plane component - reveals a drop in intensity  
 161 at the same temperature at which additional satellite reflections - modulated by a prop-  
 162 agation vector  $\mathbf{q} = (1/3\ 0\ 0)$  - appear. This suggests that the in-plane component breaks  
 163 translation symmetry upon cooling through  $T_{N2}$ . The absence of any clear anomaly in the  
 164 integrated intensities of the (020) and (110) reflections indicate that the  $c$  component of  
 165 the magnetic moments is not affected at this transition.

### 166 3.1.3 Magnetic structures

167 For the determination of the magnetic structure between  $T_{N1}$  and  $T_{N2}$  114 symmetry-  
 168 inequivalent reflections (696 unique reflections) were recorded at  $T = 220$  K. Due to the  
 169 relatively large temperature difference between the magnetic and nuclear data collection  
 170 the analysis was done by refining the nuclear and magnetic structure parameters simul-  
 171 taneously. The twin model shown in Fig. 2 was employed with the populations fixed to  
 172 the values obtained from the RT structure analysis. Symmetry analysis was employed to  
 173 derive magnetic structure models being compatible with the underlying crystal structure  
 174 and the propagation vector  $\mathbf{q} = 0$ . This task was done using the MAG2POL program and  
 175 the 4 different irreducible representations are shown in Table 2. From the basis vectors  
 176 one can deduce that only  $\Gamma_2$  yields a ferromagnetic component along the  $c$  axis within a  
 177 single Fe site ( $w$  coefficients positive for all 4 atomic positions), while revealing an anti-  
 178 ferromagnetic coupling of the components  $u$  and  $v$  within the  $a$ - $b$  plane (2 positive and  
 179 2 negative  $u/v$  coefficients). Nevertheless, all models were tested on the observed data,  
 180 but only  $\Gamma_2$  returned a good agreement. The parameters  $u$ ,  $v$  and  $w$  were constrained  
 181 to be of the same size for the 3 Fe sites within the kagome plane. This is a reasonable  
 182 assumption based on the XMCD results in [16] stating that the Fe magnetic moment at  
 183 the trigonal sites (Fe1) is larger than those in the kagome planes (Fe2-4), meaning that  
 184 the latter are closer to  $\text{Fe}^{2+}$ . In a first refinement step the  $a$  component proved to be  
 185 insignificant for all 4 sites and was set to 0 in the following. Furthermore, the refinement  
 186 procedure was very sensitive to the  $b$  component, so its absolute value was constrained

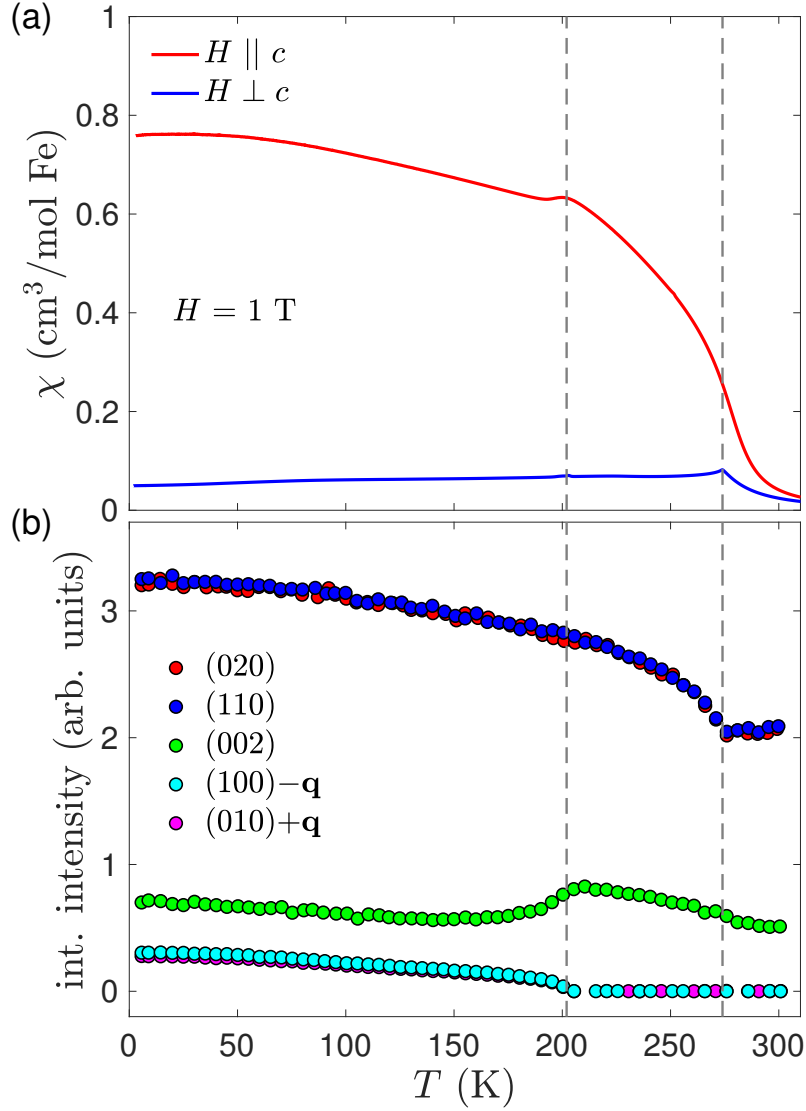


Figure 3: (a) Magnetic susceptibility measurements in a field of  $\mu_0 H = 1$  T on single crystalline  $\text{CaBaFe}_4\text{O}_7$  plotted against temperature. The curves for  $H \perp c$  and  $H \parallel c$  (taken from [16]) reveal a local maximum indicating the magnetic phase transitions at  $T_{N1} = 274$  K and  $T_{N2} = 202$  K, respectively (marked as vertical dashed lines). (b) Integrated intensities for selected integer  $(hkl)$  and satellite Bragg peaks from the D10 experiment. The anomalies in the temperature dependence correspond exactly to the magnetic phase transition temperature in (a). The evolution of the respective Bragg peak intensities allow a very good guess of the involved magnetic structures as described in the text.

Table 3: Refined magnetic parameters of the magnetic structure at 220 K and of the commensurate spin component at 2 K. The components  $\mu_b$  and  $\mu_c$  correspond to the refined parameters  $v$  and  $w$  shown in Table 2. The numbering of Fe atoms is analogous to Table 1.

Atom	$T = 220$ K		$T = 2$ K	
	$\mu_b$ ( $\mu_B$ )	$\mu_c$ ( $\mu_B$ )	$\mu_b$ ( $\mu_B$ )	$\mu_c$ ( $\mu_B$ )
Fe1	1.0(2)	3.1(1)	0.2(9)	3.68(8)
Fe2	1.0(2)	2.2(1)	0.2(9)	2.84(7)
Fe3	1.0(2)	2.2(1)	0.2(9)	2.84(7)
Fe4	1.0(2)	2.2(1)	0.2(9)	2.84(7)

187 between the Fe sites in the triangular and kagome planes. This constraint stabilized the  
 188 refinement and the agreement factor  $R_F = 4.8$ . The resulting magnetic structure can be  
 189 described as a ferrimagnetic configuration with  $\mu \parallel c$  between the Fe spins in the triangu-  
 190 lar planes and those in the kagome planes, where the larger moment of the Fe1 ion is in  
 191 agreement with the aforementioned distribution of  $\text{Fe}^{2+}$  (Fe2-4, kagome) and  $\text{Fe}^{3+}$  (Fe1,  
 192 trigonal). Furthermore, an antiferromagnetic canting of the spins is present along the  $b$   
 193 axis, which creates the classic situation of not being able to satisfy all antiferromagnetic  
 194 exchange interactions on a triangle, i.e. 2 parallel and 1 antiparallel spin. The resulting  
 195 magnetic structure is shown in Figure 4 and the refined values are shown in Table 3. It  
 196 has to be noted that a solution with a slightly worse agreement factor exists, in which  
 197 the  $b$  component is uniform within a single kagome plane. However, such a model with  
 198 satisfied ferromagnetic in-plane exchange interactions would not lead to the second mag-  
 199 netic phase transition observed at  $T_{N2}$ . A slightly reduced data set of Bragg peaks with  
 200 integer indices has been recorded within the low-temperature phase at  $T = 2$  K with  
 201 119 symmetry-inequivalent reflections (202 unique). The same refinement strategy was  
 202 applied as for the  $T = 220$  K data set, i.e. refining the nuclear structure parameters as  
 203 well as the magnetic structure components  $v$  and  $w$  within irreducible representation  $\Gamma_2$ .  
 204 We observe an increase of the  $c$  component due to the reduced temperature as well as an  
 205 insignificant  $b$  component (see Table 3), which confirms the assumption of a modulated  
 206 in-plane component. As the refinements of both nuclear and magnetic structures turn out  
 207 satisfactory, there seems to be no need of introducing a  $\text{Fe}^{2+}/\text{Fe}^{3+}$  charge ordering with  
 208 accompanying Fe-O bond-length modulations.

209 As a last step of the single-crystal experiment 1314 magnetic satellites were collected that  
 210 agree with the propagation vector  $\mathbf{q} = (1/3 \ 0 \ 0)$  at  $T = 2$  K. Symmetry-compatible mag-  
 211 netic structure models were again calculated using MAG2POL which are shown in Table 4.  
 212 Unfortunately, neither a single irreducible representation nor any mixed representation  
 213 yielded a satisfying result. This is due to the fact that nuclear scattering from additional  
 214 twin domains overlap with parts of the magnetic scattering. This is manifest by multiple  
 215 diffraction spots on the 2-dimensional detector images and multiple peaks in the  $\omega$  scans  
 216 which are impossible to resolve and to separate into individual contributions. Note that  
 217 such parasitic scattering was not observed in the rocking scans of integer reflections. It  
 218 is therefore not possible to confidently extract the magnetic intensities and to analyze  
 219 the modulated part of the low-temperature magnetic phase from our single-crystal data.  
 220 A polarized neutron approach using spherical neutron polarimetry - as employed for the  
 221 related  $\text{CaBa}(\text{Co}_3\text{Fe})\text{O}_7$  compound [27], failed due to the strong ferrimagnetic component  
 222 throughout the whole magnetically ordered temperature range despite the effort of prior  
 223 cooling in a magnetic field (in order to reduce neutron depolarization between magnetic  
 224 domains) and focusing only on incident and final neutron polarization states parallel to

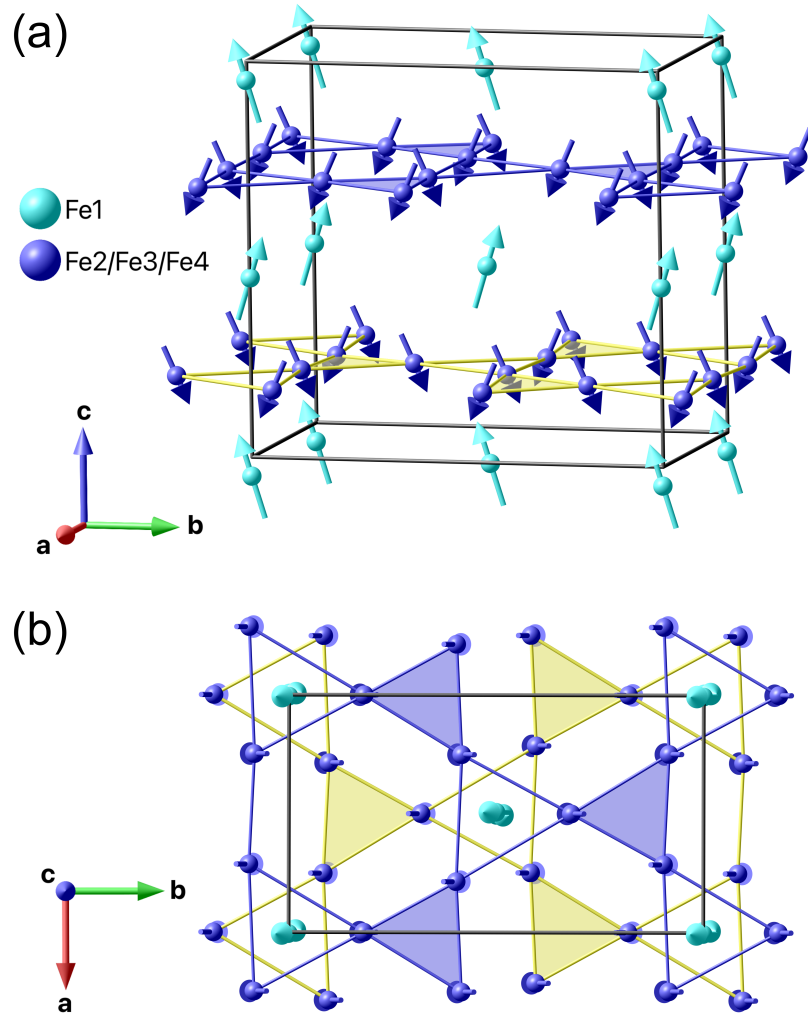


Figure 4: (a) Perspective view of the magnetic structure in  $\text{CaBaFe}_4\text{O}_7$  at 220 K. Only the magnetic ions on the triangular (light blue) and hexagonal sites (dark blue) are shown. Bonds between Fe ions in the kagome planes are drawn as a guide to the eye. The kagome plane at  $z \sim 0.2$  is emphasized in yellow in order to be distinguished from the one at  $z \sim 0.7$ .  $T_1$  triangles are open, while  $T_2$  triangles are filled. (b) View along the  $c$  axis emphasizing the  $b$  component of the magnetic moments. All Fe triangles in the kagome plane reveal 2 spins pointing along the positive (negative)  $b$  axis, while 1 spin is pointing along the negative (positive)  $b$  axis.



Table 4: Basis vectors  $\psi_n$  of the irreducible representation  $\Gamma_n$  for each of the Fe sites of  $\text{CaBaFe}_4\text{O}_7$  for space group  $Pbn2_1$  and propagation vector  $\mathbf{q} = (1/3 \ 0 \ 0)$ . Note that each of the Fe sites splits into two orbits. The phase factor  $a = \exp(2\pi i\mathbf{q}\mathbf{r})$  results from the  $n$  glide plane perpendicular to the  $b$  axis with translation vector  $\mathbf{r} = (1/2 \ 0 \ 1/2)$

Atom	Position	$\psi_1$	$\psi_2$
1	$\begin{pmatrix} x \\ y \\ z \end{pmatrix}$	$\begin{pmatrix} u \\ v \\ w \end{pmatrix}$	$a \cdot \begin{pmatrix} \bar{u} \\ v \\ \bar{w} \end{pmatrix}$
2	$\begin{pmatrix} x + 1/2 \\ \bar{y} + 1/2 \\ z + 1/2 \end{pmatrix}$	$\begin{pmatrix} u \\ v \\ w \end{pmatrix}$	$a \cdot \begin{pmatrix} u \\ \bar{v} \\ w \end{pmatrix}$

225 the ferrimagnetic component (longitudinal polarization analysis).

### 226 3.2 Powder neutron diffraction

227 Due to the difficulties in deriving the low-temperature in-plane component encountered in  
 228 the single-crystal experiment we now turn to our powder neutron diffraction data in order  
 229 to address this remaining issue. The sequence of magnetic phase transitions coincides with  
 230 the results above which is shown in the following.

231 All recorded diffraction patterns between 15 K and 300 K were used to construct the  
 232 thermodiffractogramm depicted in Figure 5. The transition into the canted ferrimagnetic  
 233 structure at  $T_{N1}$  is marked by the increase of commensurate reflections e.g. at scattering  
 234 angles  $26.8^\circ$ ,  $30.4^\circ$  and  $39.4^\circ$ . The onset of the modulated phase at  $T_{N2}$  is accompanied by  
 235 the appearance of magnetic satellites from which the strongest are located at  $2\theta = 15.4^\circ$   
 236 and  $21.0^\circ$ . Note that the positions of the satellites do not change with temperature. A  
 237 few selected Bragg reflections at positions with integer and non-integer Miller indices were  
 238 integrated using a Gaussian profile on a sloping background in all diffraction patterns which  
 239 were used to construct the color map in Figure 5. The resulting temperature dependence  
 240 of integrated intensities is shown in Figure 6. The first transition, at  $T_{N1}$ , can only be  
 241 interpreted as a jump of the (020), (110) (at  $2\theta = 26.7^\circ$  and  $26.8^\circ$ , respectively) and  
 242 (111) ( $2\theta = 30.4^\circ$ ) intensities between 300 K and 270 K due to the lack of recorded data  
 243 within this temperature range. The integrated intensities of the satellites (010)+ $\mathbf{q}$  ( $2\theta =$   
 244  $15.4^\circ$ ) and (101)+ $\mathbf{q}$  ( $2\theta = 21.0^\circ$ ) show a significant increase below 210 K. Both transition  
 245 temperatures match very well with the more detailed picture shown in Figure 3(b) derived  
 246 from the single-crystal sample.

247 As a first step the diffraction pattern at RT was analyzed in order to refine the nuclear  
 248 structure parameters, an overall isotropic temperature factor and the scale factor. The  
 249 observed pattern can nicely be described using the known structure ( $R_F = 8.2$ ) which is  
 250 shown in Figure 7(a). The resulting structural model was used as a starting point for the  
 251 analysis of the 15 K pattern. The scale factor was left unchanged and only the lattice  
 252 parameters and the overall isotropic temperature factor were refined in order to guarantee  
 253 the correct position and scaling of the magnetic satellites. The propagation vector was  
 254 refined to  $\mathbf{q} = [0.3354(5) \ 0 \ 0]$ . Figure 7(b) zooms on the low- $Q$  part of the diffraction  
 255 pattern containing the clearly visible magnetic satellites. Apart from the two strongest  
 256 magnetic Bragg peaks already visible in the thermodiffractogramm the relatively weak  
 257 fundamental reflection (000)+ $\mathbf{q}$  can be seen at  $2\theta = 7.7^\circ$  as well as a series of peaks  
 258 between  $32^\circ$  and  $45^\circ$ . The strong nuclear reflections as well as parasitic peaks observable

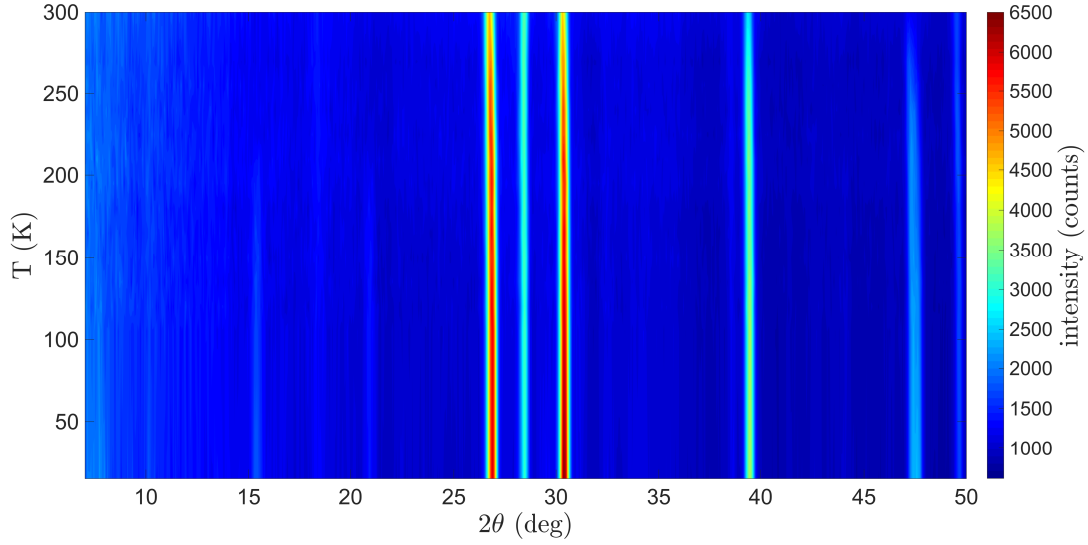


Figure 5: Thermodiffractogram showing the magnetic phase transitions at  $T_{N1} = 274$  K and  $T_{N2} = 204$  K (note that the temperature values were derived from the single-crystal experiments). The onset of the commensurate ferrimagnetic structure is manifest by an increase of intensity on e.g. the reflections at  $2\theta$  values of  $26.8^\circ$ ,  $30.4^\circ$  and  $39.4^\circ$ . The transition into the low-temperature magnetic phase is accompanied by the appearance of new satellite peaks, e.g. at  $2\theta = 15.4^\circ$  and  $21.0^\circ$ .

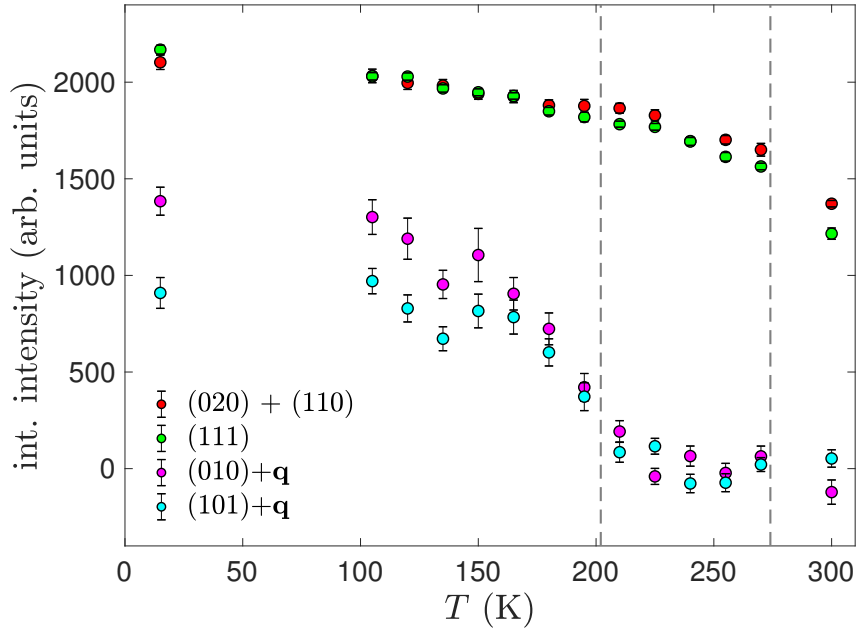


Figure 6: Integrated intensities of selected Bragg reflections at positions with integer and non-integer Miller indices, the latter being modulated by the propagation vector  $\mathbf{q} = (1/3 \ 0 \ 0)$ . The (020) and (110) reflections can not be separated due to their very similar scattering angle ( $2\theta = 26.7^\circ$  and  $26.8^\circ$ , respectively), but both reveal a significant magnetic contribution which results in a comparable temperature dependence as the single peak (111) at  $2\theta = 30.4^\circ$ . The magnetic satellites show an increase in intensity upon cooling below approximately 200 K. The transition temperatures derived from the single-crystal experiments (cf. Fig. 3) are shown as vertical dashed lines.

Table 5: Refined magnetic parameters of the modulated in-plane magnetic structure component at 15 K ( $R_F = 12.7$ ). The numbering of Fe atoms is analogous to Table 1 and the positions of the primed Fe atoms are related to the unprimed ones by the  $b$  glide plane lost in the transition.

Atom	$\mu_a$ ( $\mu_B$ )	$\mu_b$ ( $\mu_B$ )	$\varphi/(2\pi)$
Fe1	1.6(3)	1.6(3)	0
Fe1'	1.6(3)	1.6(3)	0.04(3)
Fe2	1.6(1)	1.6(1)	0.09(3)
Fe2'	1.6(1)	1.6(1)	0.77(3)
Fe3	1.6(1)	1.6(1)	$\varphi(Fe2') + 1/3$
Fe3'	1.6(1)	1.6(1)	$\varphi(Fe2) + 1/3$
Fe4	1.6(1)	1.6(1)	$\varphi(Fe2) - 1/3$
Fe4'	1.6(1)	1.6(1)	$\varphi(Fe2') - 1/3$

259 at all temperatures (e.g. at  $10.3^\circ$  and  $18.4^\circ$  in  $2\theta$ ) were excluded from the refinement.

260 The irreducible representations listed in Table 4 were used, however, the complexity of  
 261 the nuclear and magnetic structure in combination with the limited number of observed  
 262 magnetic reflections requires reasonable constraints and starting parameters to assure  
 263 refinement stability. Since the Fe sites split into two orbits due to the reduced propagation  
 264 vector symmetry and each site features an  $a$  and  $b$  component as well as a phase factor,  
 265 the maximum number of magnetic structure parameters is 23 (note that the phase of  
 266 one Fe site needs to be fixed). Therefore, as already applied in the analysis of the high-  
 267 temperature magnetic phase the size of the  $a$  and  $b$  component was constrained to be the  
 268 same for Fe spins on the same type of site, i.e. within the triangular or kagome planes.  
 269 As a starting point of the refinement process different classical spin configurations on a  
 270 kagome lattice were introduced on the Fe triangles in the kagome plane - including  $120^\circ$   
 271 spin arrangements on the  $T_1$  and/or  $T_2$  triangles - by fixing the respective phase factors,  
 272 which were then refined within either  $\Gamma_1$ ,  $\Gamma_2$ ,  $\Gamma_1 + \Gamma_2$  symmetry or without symmetry  
 273 constraints.

274 A very convincing solution was found by constraining only the  $T_1$  triangles to reveal  
 275 a  $120^\circ$  spin arrangement within  $\Gamma_1$  symmetry. The phase factors between two triangles  
 276 separated along the  $z$  axis as well as between the triangular Fe spins were refined together  
 277 with the spin envelope in the  $a$ - $b$  plane for triangular and kagome sites. After the first  
 278 refinement steps the  $a$  and  $b$  components of both Fe types revealed similar values for which  
 279 the spin envelope was constrained to be circular reducing the total number of refinable  
 280 parameters to 5. We obtain an agreement factor of  $R_F = 12.7$  and the good agreement  
 281 between the calculated and observed patterns can be seen in Figure 7(b), the refined pa-  
 282 rameters are listed in Table 5. The circular spin envelope with an amplitude of  $1.6 \mu_B$  at  
 283 15 K matches very well with the collinear  $b$  component of  $1.0 \mu_B$  which was determined  
 284 at an elevated temperature of  $T = 220$  K.

285 Apart from the same spin envelope for all sites it is obvious that the refined phase factor  
 286 between the Fe2' and Fe2 spin is close to  $2\pi/3$  and the one between Fe1' and Fe1 is almost  
 287 zero. Therefore, in principle, the magnetic structure could be described with only 2 free  
 288 parameters, which are an overall moment amplitude and the phase factor between the  
 289 kagome and triangular planes. Such a minimal model still yields  $R_F = 13.7$  compared to  
 290  $R_F = 12.7$  with 5 parameters. The commensurate component along the  $c$  axis together  
 291 with the cycloidal component within the  $a$ - $b$  plane results in a conical magnetic structure  
 292 which is depicted in Figure 8 and will be discussed in the following section.

293

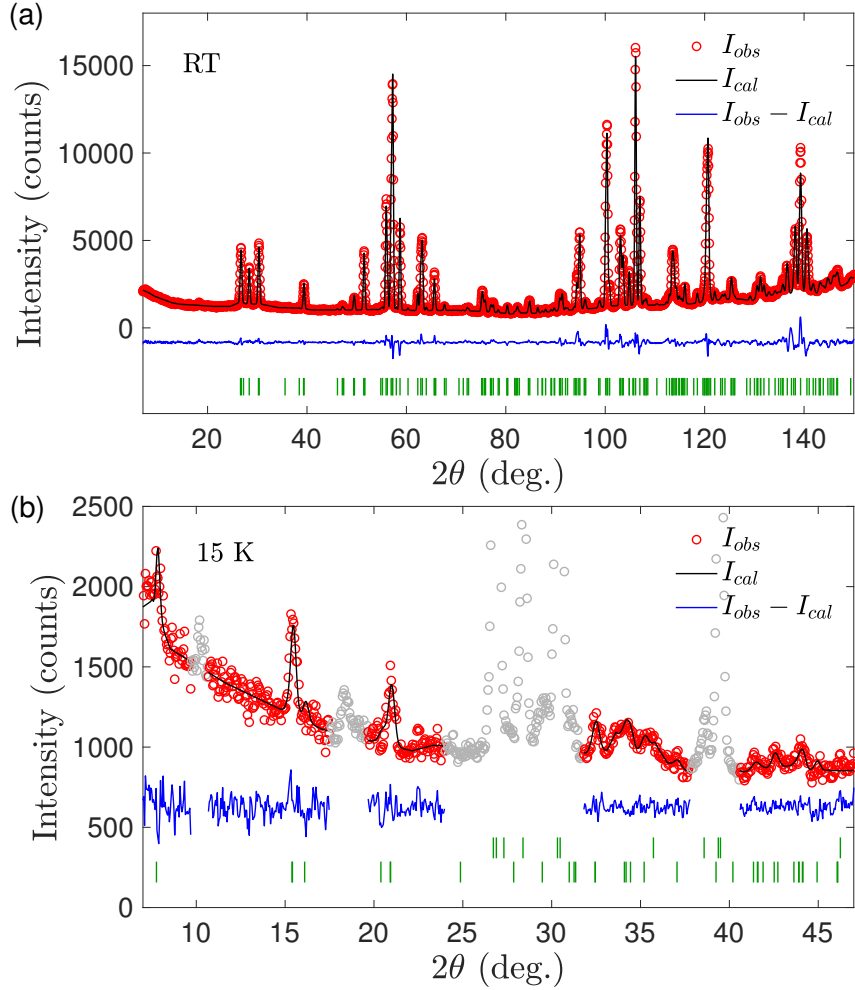


Figure 7: Observed [(red) dots] and calculated [(black) solid line] diffraction patterns at (a) RT and (b) 15 K with the difference curve shown (in blue) at the bottom. In (a) the (green) markers indicate the position of nuclear Bragg peaks within the  $Pbn2_1$  space group. In (b) the first row of (green) markers denotes the position of nuclear Bragg peaks, while the second row indicates the positions of magnetic Bragg peaks with the propagation vector  $\mathbf{q}=(1/3\ 0\ 0)$ . Gray data points show the regions which were excluded from the fit for containing either nuclear peaks or parasitic peaks also present above the magnetic ordering temperatures.

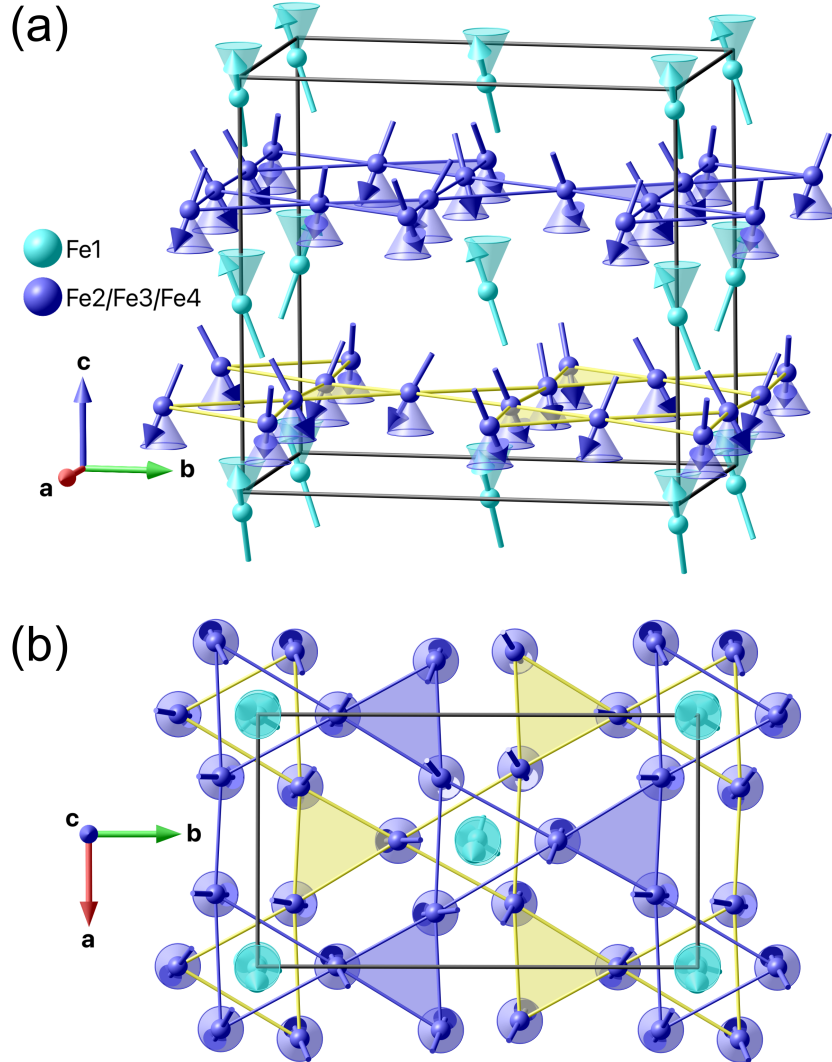


Figure 8: (a) Perspective view of the conical ferrimagnetic structure in  $\text{CaBaFe}_4\text{O}_7$  at 15 K. Only the magnetic ions on the triangular (light blue) and hexagonal sites (dark blue) are shown. The conical envelope of the magnetic moments as well as bonds between Fe ions in the kagome planes are drawn as a guide to the eye. The kagome plane at  $z \sim 0.2$  is emphasized in yellow in order to be distinguished from the one at  $z \sim 0.7$ .  $T_1$  triangles are open, while  $T_2$  triangles are filled. (b) View along the  $c$  axis emphasizing the rotation of the magnetic moments within the  $a$ - $b$  plane. The spin rotation plane is emphasized by disks in the respective colors. The triangular plaquettes  $T_1$  of kagome Fe spins reveals a  $120^\circ$  configuration. The same spin orientation and triangular chirality is found for the triangle at  $\Delta z = 0.5$  indicating a ferromagnetic coupling between two plaquettes.

294 **4 Conclusion**

295 We have presented a combination of magnetic susceptibility and neutron diffraction ex-  
296 periments on powder and single-crystal samples which address the magnetic phases in  
297 the  $\text{CaBaFe}_4\text{O}_7$  compound and reveal yet another type of magnetic ordering adding to  
298 the rich diversity of examples within the Swedenborgite family. All employed techniques  
299 reveal two magnetic phase transitions, the first at  $T_{N1} = 274$  K into a ferrimagnetic struc-  
300 ture with antiferromagnetic canting perpendicular to the easy direction, and the second at  
301  $T_{N2} = 202$  K where the in-plane component changes from a collinear to a cycloidal arrange-  
302 ment which results in a conical magnetic structure at low temperatures. This sequence of  
303 magnetic phase transitions is an excellent example of the temperature-dependent compe-  
304 tition between single-ion anisotropy and exchange interactions. In the high-temperature  
305 phase the collinear  $b$  component creates the textbook situation of two parallel and one  
306 antiparallel spins on a triangle, the prototypic example of geometric frustration. Between  
307 274 K and 202 K the spin Hamiltonian seems to be dominated - at least for the in-plane  
308 component - by the single-ion anisotropy which reduces the system's energy by canting  
309 the spins along the  $b$  axis. However, when the temperature is lowered the frustrated anti-  
310 ferromagnetic exchange interaction become more important for which a spin reorientation  
311 takes place towards a partial  $120^\circ$  degrees arrangement. The in-plane component of this  
312 complex structure can be appreciated in Figure 8(b) by viewing it along the  $c$  axis. One  
313 can see that the same  $120^\circ$  spin configuration is present on two  $T_1$  triangles, above as  
314 well as below a triangular Fe spin. Apart from the antiferromagnetic coupling within each  
315 of those triangles such a structure suggests a ferromagnetic exchange interaction between  
316 two triangular plaquettes along the  $c$  axis. This seems to be the decisive characteristic  
317 of the magnetic structure, because a spin configuration which yields a  $120^\circ$  alignment  
318 on all triangles - which does not explain the experimental data - requires an opposite  
319 triangular chirality between two  $T_1$  triangles separated by  $z \sim 0.5$ . Consequently, the  
320  $T_2$  triangles do not show an apparent coupling scheme for which we conclude that the  
321 exchange interactions within those triangles play a minor role in the spin Hamiltonian  
322 of this Swedenborgite compound. The structural origin of the different ordering schemes  
323 between  $T_1$  and  $T_2$  triangles presumably lies in the vicinity of the triangular Fe spins  
324 which cap the  $T_1$  triangles above and below, which therefore leads to a different balance  
325 of exchange interactions. The bare presence of a canted ferrimagnetic order is proof for a  
326 strong coupling between the planes, and a cluster consisting of ferromagnetically ordered  
327  $T_1$  triangles with apparent  $120^\circ$  order within the plaquettes above and below a triangular  
328 Fe spin suggests that the resulting magnetic structure is governed by the superexchange  
329 interactions within these units. In contrast, the magnetic interactions between the clusters  
330 (note that a  $T_2$  triangle constitutes the intersection of 3 clusters) are not perfectly fulfilled  
331 and - in turn - are less dominant in the energy balance, which may be related to the fact  
332 that  $T_2$  triangles are structurally more isolated due to the absence of another  $T_2$  triangle  
333 along the  $c$  direction.

334 On the other hand it is not quite clear why the system reveals a small in-plane component  
335 besides the strong ferrimagnetic component along the  $c$  axis and how the low-temperature  
336 magnetic structure is responsible for inducing a ferroelectric polarization when applying  
337 a magnetic field. Whether the microscopic origin of this near-room-temperature multifer-  
338 roic is magnetostriction, the spin-current mechanism or Fe-O orbital hybridization, as put  
339 forward by Kocsis *et al.* [17], is still an open debate. The precise Fe-O-Fe bond distances  
340 and angles between the triangular and kagome layers, as well as within the  $T_1$  and  $T_2$   
341 triangles, as a function of temperature would certainly reveal valuable information about  
342 this remaining question, but this is beyond the possibilities of the data at hand. Further



343 investigations, e.g. using high-resolution X-ray synchrotron diffraction, are required to  
344 reveal the structural origin of the observed magnetic structures. For a more precise pic-  
345 ture of the energy balance in the spin Hamiltonian additional inelastic neutron scattering  
346 studies would be necessary based on the structural and magnetic properties provided in  
347 this work. Nevertheless, the details of the complex magnetic order at low temperatures  
348 combined with the magnetoelectric data [17] may stimulate further *ab initio* calculations  
349 in order to provide a solid base for the understanding of the magnetoelectric effect in this  
350 system.

351

## 352 Acknowledgements

353 **Funding information** This work was supported by the German Science Foundation  
354 (DFG) through SFB608 and SFB1143.

## 355 References

- 356 [1] A. P. Ramirez, *Strongly geometrically frustrated magnets*, Annu. Rev. Mater. Sci. **24**,  
357 453 (1994), doi:10.1146/annurev.ms.24.080194.002321.
- 358 [2] R. Moessner and A. P. Ramirez, *Geometrical frustration*, Phys. Today **59**, 24 (2006),  
359 doi:10.1063/1.2186278.
- 360 [3] M. R. Norman, *Colloquium: Herbertsmithite and the search for the quantum spin*  
361 *liquid*, Rev. Mod. Phys. **88**, 041002 (2016), doi:10.1103/RevModPhys.88.041002.
- 362 [4] P. Mendels and F. Bert, *Quantum kagome frustrated antiferromagnets: One route to*  
363 *quantum spin liquids*, C. R. Phys. **17**, 455 (2016), doi:10.1016/j.crhy.2015.12.001.
- 364 [5] M. J. Harris and M. P. Zinkin, *Frustration in the pyrochlore antiferromagnets*, Mod.  
365 Phys. Lett. B **10**, 417 (1996), doi:10.1142/S021798499600047X.
- 366 [6] J. G. Rau and M. J. P. Gingras, *Frustrated quantum rare-earth pyrochlores*,  
367 Annu. Rev. Condens. Matter Phys. **10**, 357 (2019), doi:10.1146/annurev-conmatphys-  
368 022317-110520.
- 369 [7] M. Valldor and M. Andersson, *The structure of the new compound  $YBaCo_4O_7$  with a*  
370 *magnetic feature*, Solid State Sci. **4**, 923 (2002), doi:10.1016/s1293-2558(02)01342-0.
- 371 [8] G. Aminoff, *Über ein neues Mineral von längban (swedenborgit)*, Z. Krist **60**, 262  
372 (1924).
- 373 [9] G. Aminoff and R. Blix, Kgl. Sv. Vet. H. **11**, 1 (1933).
- 374 [10] M. Valldor, *Disordered magnetism in the homologue series  $YBaCo_{4-x}Zn_xO_7$  ( $x$*   
375 *= 0, 1, 2, 3)*, J. Phys.: Condens. Matter **16**, 9209 (2004), doi:10.1088/0953-  
376 8984/16/50/012.
- 377 [11] A. Huq, J. F. Mitchell, H. Zheng, L. C. Chapon, P. G. Radaelli, K. S. Knight and  
378 P. W. Stephens, *Structural and magnetic properties of the kagomé antiferromagnet*  
379  *$YbBaCo_4O_7$* , J. Solid State Chem. **179**, 1136 (2006), doi:10.1016/j.jssc.2006.01.010.

- 380 [12] V. Markus, K. Maarit, M. Teruki, L. Ru-Shi, C. Jin-Ming and Y. Hisao, *In situ*  
381 *and ex situ monitoring of oxygen absorption in  $YBaCo_4O_{7+\delta}$* , Chem. Lett. **36**, 1368  
382 (2007), doi:10.1246/cl.2007.1368.
- 383 [13] V. Caignaert, A. Maignan, K. Singh, C. Simon, V. Pralong, B. Raveau, J. F. Mitchell,  
384 H. Zheng, A. Huq and L. C. Chapon, *Gigantic magnetic-field-induced polarization*  
385 *and magnetoelectric coupling in a ferrimagnetic oxide  $CaBaCo_4O_7$* , Phys. Rev. B **88**,  
386 174403 (2013), doi:10.1103/PhysRevB.88.174403.
- 387 [14] R. S. Fishman, S. Bordács, V. Kocsis, I. Kézsmárki, J. Viirok, U. Nagel, T. Rõõm,  
388 A. Puri, U. Zeitler, Y. Tokunaga, Y. Taguchi and Y. Tokura, *Competing exchange*  
389 *interactions in multiferroic and ferrimagnetic  $CaBaCo_4O_7$* , Phys. Rev. B **95**, 024423  
390 (2017), doi:10.1103/PhysRevB.95.024423.
- 391 [15] B. Raveau, V. Caignaert, V. Pralong, D. Pelloquin and A. Maignan, *A series of novel*  
392 *mixed valent ferrimagnetic oxides with a  $T_c$  up to 270 K:  $Ca_{1-x}Y_xBaFe_4O_7$* , Chem.  
393 Mater. **20**, 6295 (2008), doi:10.1021/cm8018692.
- 394 [16] N. Hollmann, M. Valldor, H. Wu, Z. Hu, N. Qureshi, T. Willers, Y.-Y. Chin, J. C.  
395 Cezar, A. Tanaka, N. B. Brookes and L. H. Tjeng, *Orbital occupation and magnetism*  
396 *of tetrahedrally coordinated iron in  $CaBaFe_4O_7$* , Phys. Rev. B **83**, 180405(R) (2011),  
397 doi:10.1103/PhysRevB.83.180405.
- 398 [17] V. Kocsis, Y. Tokunaga, S. Bordács, M. Kriener, A. Puri, U. Zeitler, Y. Taguchi,  
399 Y. Tokura and I. Kézsmárki, *Magnetoelectric effect and magnetic phase dia-*  
400 *gram of a polar ferrimagnet  $CaBaFe_4O_7$* , Phys. Rev. B **93**, 014444 (2016),  
401 doi:10.1103/PhysRevB.93.014444.
- 402 [18] S.-W. Cheong and M. Mostovoy, *Multiferroic: a magnetic twist for ferroelectricity*,  
403 Nat. Mater. **6**, 13 (2007), doi:10.1038/nmat1804.
- 404 [19] M. Fiebig, T. Lottermoser, D. Meier and M. Trassin, *The evolution of multiferroics*,  
405 Nat. Rev. Mater. **1**, 16046 (2016), doi:10.1038/natrevmats.2016.46.
- 406 [20] N. D. Mermin and H. Wagner, *Absence of ferromagnetism or antiferromagnetism*  
407 *in one- or two-dimensional isotropic Heisenberg models*, Phys. Rev. Lett. **17**, 1133  
408 (1966), doi:10.1103/PhysRevLett.17.1133.
- 409 [21] N. Qureshi, B. Ouladdiaf, A. Senyshyn, V. Caignaert and M. Valldor, *Non-collinear*  
410 *magnetic structures in the Swedenborgite  $CaBaFe_4O_7$  derived by powder and single-*  
411 *crystal neutron diffraction*, Institut Laue-Langevin and Forschungs-Neutronenquelle  
412 Heinz Maier-Leibnitz (FRM-II) (2009), doi:10.5281/zenodo.5783436.
- 413 [22] Heinz Maier-Leibnitz Zentrum, *Spodi: High resolution powder diffractometer*, JLSRF  
414 **1**, A5 (2015), doi:10.17815/jlsrf-1-24.
- 415 [23] N. Qureshi, *Mag2Pol: A program for the analysis of spherical neutron polarime-*  
416 *try, flipping ratio and integrated intensity data*, J. Appl. Cryst. **52**, 175 (2019),  
417 doi:10.1107/S1600576718016084.
- 418 [24] J. Rodríguez-Carvajal, *Recent advances in magnetic structure determination by neu-*  
419 *tron powder diffraction*, Physica B **192**, 55 (1993), doi:10.1016/0921-4526(93)90108-I.
- 420 [25] G. M. Sheldrick, *A short history of shelx*, Acta Crystallogr., Sect. A: Found. Cryst.  
421 tallogr. **64**, 112 (2008), doi:10.1107/S0108767307043930.

- 422 [26] R. S. Perry, H. Kurebayashi, A. Gibbs and M. J. Gutmann, *Crystal structure and*  
423 *crystal growth of the polar ferrimagnet  $\text{CaBaFe}_4\text{O}_7$* , Phys. Rev. M **2**, 054403 (2018),  
424 doi:10.1103/PhysRevMaterials.2.054403.
- 425 [27] N. Qureshi, M. T. Fernandez-Díaz, L. Chapon, A. Senyshyn, W. Schweika and  
426 M. Valldor, *Magnetic structure of the swedenborgite  $\text{CaBa}(\text{Co}_3\text{Fe})\text{O}_7$  derived by un-*  
427 *polarized neutron diffraction and spherical neutron polarimetry*, Phys. Rev. B **97**,  
428 064404 (2018), doi:10.1103/PhysRevB.97.064404.